ACS APPLIED MATERIALS & INTERFACES

Research Article

Cite This: ACS Appl. Mater. Interfaces 2019, 11, 28423−28430

www.acsami.org

High-Efficiency Metalenses with Switchable Functionalities in Microwave Region

Kuang Zhang,*[,†,§] Yueyi Yuan,[†] Xumin Ding,*[,†,§] Badreddine Ratni,[‡] Shah Nawaz Burokur,*[,‡] and Qun Wu[†]

[†]Department of Microwave Engineering, Harbin Institute of Technology, Harbin 150001, China

[‡]LEME, UPL, Univ Paris Nanterre, F92410 Ville d'Avray, France

[§]Key Laboratory of Millimeter Waves, Nanjing 210096, China

Supporting Information

ABSTRACT: Regarding miniaturized and integrated systems, a single flat device that possesses diversified functionalities is highly desirable in optical to microwave regimes. With this perspective, bifunctional metalenses constructed by meta-atoms with integrated response to propagation phase and geometric phase are proposed for independent manipulation of right-handed and left-handed circularly polarized waves. The derived general criterion is verified in the microwave region from three bifunctional metalenses operating in transmission manner. The proof-of-concept measurements show that all these metalenses exhibit two independent functionalities that can be switched by flipping the helicity of the incident illumination. Very high efficiencies of around 80%, with peak value of 91%, are achieved by the ultrathin metasurfaces of thickness $0.15\lambda_0$. The proposed metasurfaces provide a promising route for the realization of reconfigurable lenses and antennas in wireless communication systems.

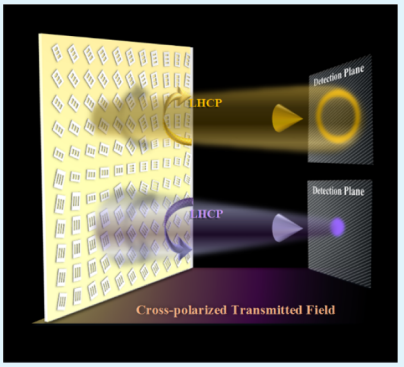

KEYWORDS: *metalenses, high efficiency, propagation phase, geometric phase, switchable functionality, microwave region*

INTRODUCTION

Metasurface, referring to thin planar arrangement of artificial meta-atoms in the subwavelength scale, has exhibited versatile abilities in manipulating the phase, magnitude, and polarization of electromagnetic (EM) waves.[1−7] Metasurface in optical and terahertz region offers a new paradigm for applications in flat lenses,[8−11] spin-to-orbit conversion,[12−15] digital holograms,[16−20] hybrid coupled plasmonic system based on graphene,[21] dynamic modulation of EM wavefront,[22−27] to name a few. With diverse functionalities and ultrathin thickness, metasurfaces are also promising and widely utilized in radio frequency region, for radar cross section reduction,[28,29] spoof surface plasmon polaritons,[30] tunable retroreflection,[31] detection imaging,[32,33] biomedical diagnosis and treatment,[33−35] cloaking,[36,37] high-gain and beam-steering antennas,[38,39] and generation of orbital angular momentum (OAM) modes for wireless communication systems.[40−42]

With the increasing requirement of miniaturized and highly integrated systems, single metasurface exhibiting multiple functionalities is desirable for reconfigurable lens antennas in wireless communication systems. To switch between functionalities, the polarization state of incident wave would be a convenient and feasible trigger for metasurface plateau. For linearly polarized incident waves, numerous works have been presented based on the propagation phase principle by adjusting the geometrical dimensions of each anisotropic meta-atom to obtain different responses for orthogonal linear polarizations.[43−47] On the other hand, for circularly polarized (CP) incident waves, geometric phase, also named as the Pancharatnam−Berry (P−B) phase, has been widely explored for metasurface design to flexibly manipulate EM wavefronts.[48−52] Nevertheless, the intrinsic nature of the P−B phase produces antisymmetrical (equal and opposite) response characteristics between orthogonal CP states,[52] which means that the right-handed and left-handed circularly polarized (RHCP and LHCP) waves cannot be independently manipulated by applying the spatial phase function achieved with only the geometric phase.

To overcome this limitation, a direct method involves combining two sets of meta-atoms together, where each set of meta-atoms exhibits specific phase response to only one CP incident wave, such that different functions can be achieved by switching the polarization state of the incidence.[18,53,54] However, mutual interferences between the two sets of meta-atoms will inevitably affect both functionalities and their efficiencies. Recently, it has been demonstrated that the orthogonal polarization states of the wavefronts can be modulated independently by synthesizing the propagation phase and geometrical phase.[55] Arbitrary spin angular momentum (SAM) to orbital angular momentum (OAM)

Received: April 23, 2019
Accepted: July 12, 2019
Published: July 12, 2019

DOI: 10.1021/acsami.9b07102
ACS Appl. Mater. Interfaces 2019, 11, 28423−28430

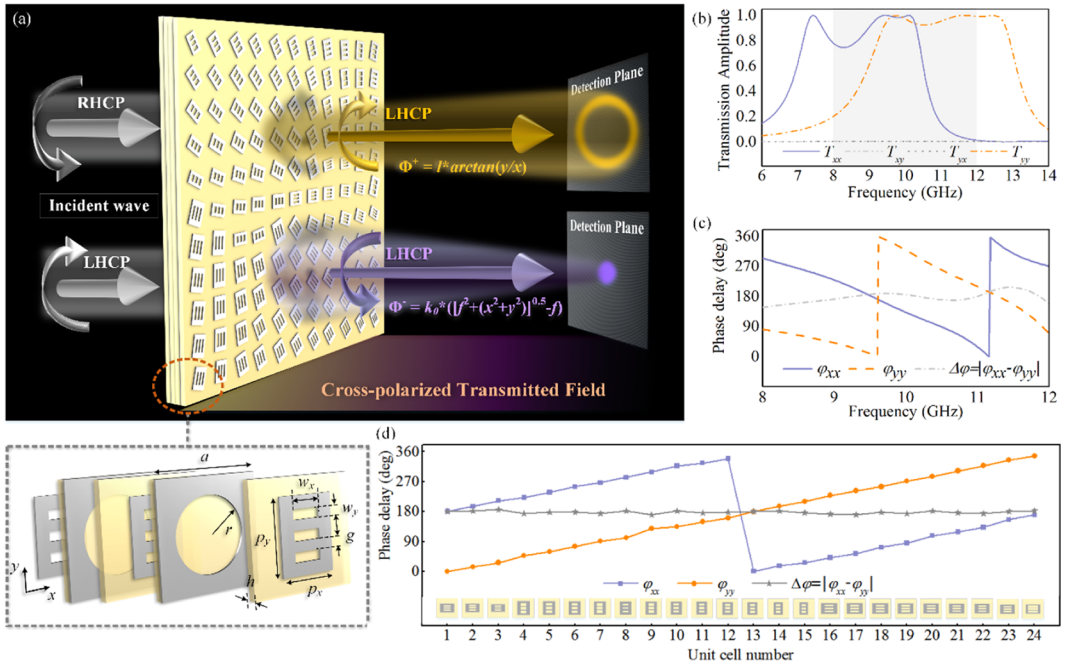

Figure 1. (a) Schematic demonstration of a metasurface to independently manipulate the cross-polarized transmitted wave with opposite handedness. The inset shows the topological layouts of the proposed meta-atom, where the periodicity a of the meta-atom equals 8.8 mm; radius of the circular aperture in the grid layer is r = 3 mm; thickness of each dielectric substrate is h = 1 mm; p_x and p_y are the length and width of the metallic patch; w_x and w_y are the dimensions of the rectangular gap in the metallic patch; and g is the distance between two adjacent gaps. (b) Simulated transmission magnitude and (c) phase spectrum of the representative meta-atom. (d) Twenty-four meta-atoms designed and optimized to cover the full 2π phase range with $\pi/12$ interval.

converter has been proposed,[56] and independent beam refraction and optical hologram imaging for opposite circular polarizations has been realized in the visible spectrum.[57,58] To exhibit high efficiency and full phase coverage of 2π simultaneously, three-dimensional dielectric meta-atoms such as rectangular pillars and elliptical posts were proposed in the optical region. Due to the fabrication and inherent response limitation, their nonplanar profiles usually have thickness close to or more than the working wavelength λ_0,[16,54,55,58] and these dielectric metastructures are generally preset to work at a specific wavelength[55,56] or exhibit high efficiency within a narrow bandwidth.[57,58]

In this paper, metalenses with switchable functionalities are achieved in the microwave region by involving the combination of geometric and propagation phases. A good trade-off is obtained between efficiency, thickness, and bandwidth, which are the three key factors for the application of metasurfaces in reconfigurable antennas for wireless or satellite communication systems. Three bifunctional ultrathin metasurfaces with thickness of $0.15\lambda_0$ are constructed by miniaturized planar meta-atoms to operate in a transmission manner under orthogonal CP incident wave as (1) bifocal metalens, (2) dual-mode orbital angular momentum (OAM) generator, and (3) switchable converging metalens/OAM generator. Numerical simulations and proof-of-concept experiments show that the proposed metasurfaces are able to generate two independent and arbitrary functionalities with relatively high efficiencies, which can be switched by flipping the helicity of the incident wave. Our achieved results provide a method to realize high-efficiency flat metadevices with integrated multifunctionalities, which may open the way to applications in modern communication systems.

RESULTS AND DISCUSSION

Basic Principle and Meta-Atom Design. The schematic principle of the proposed independent manipulation of orthogonal circularly polarized incident wave is shown in Figure 1a. To achieve switchable functionalities by flipping the helicity of incidence, the inherent relationship between LHCP and RHCP should be decoupled, which can be realized by the synthesis of geometric and propagation phases. For a meta-atom without chirality, the propagation phase can be adjusted through the geometric dimensions of the meta-atom and exhibits a symmetrical response (equal and same response) to LHCP and RHCP incident wave illuminations, while the geometric phase can be tuned by the relative rotation angle of the meta-atom and shows an antisymmetrical response (equal and opposite response) to LHCP and RHCP incident wave illuminations. Thus, by tuning the geometric size and rotation angle of the meta-atom simultaneously, the propagation phase can be introduced to combine with the geometric phase, resulting in totally different phase responses under LHCP and RHCP illuminations, which will further lead to switchable functionalities of the metalens by flipping the helicity of the incidence. To achieve the desired functionality, spatial phase distributions integrated into the metalens need to be fixed, which is the first step in the design approach of the metasurface. Jones matrix, exhibiting the relationship between transmitted and incident waves, is adopted to derive the general requirement of the propagation phase and geometric phase.

It is supposed that incident waves are either in the LHCP state $|\lambda^+\rangle = |L\rangle = \begin{bmatrix}1\\ i\end{bmatrix}$ or the RHCP state $|\lambda^-\rangle = |R\rangle = \begin{bmatrix}1\\ i\end{bmatrix}$. The transmitted output wave would carry an opposite handedness $|(\lambda^+)^*\rangle$ or $|(\lambda^-)^*\rangle$ and acquire a spatial phase

DOI: 10.1021/acsami.9b07102
ACS Appl. Mater. Interfaces 2019, 11, 28423−28430

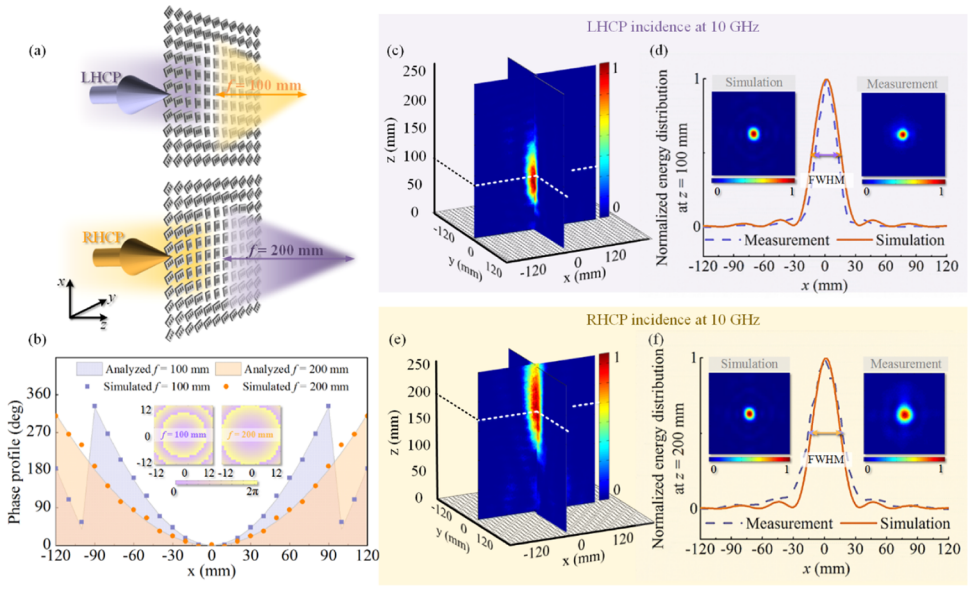

Figure 2. Bifocal converging metalens. (a) Schematic principle of proposed converging metalens, which can focus orthogonal circular polarized incidence with focal length of f_1 = 100 mm and f_2 = 200 mm, respectively. (b) Calculated and simulated spatial phase profiles for converging orthogonal CP incidence. Measured energy distribution in both *xoz* and *yoz* planes under (c) LHCP and (e) RHCP incident waves, respectively. Simulated and measured horizontal cuts of the focal spot in the *xoy* plane at (d) z = 100 mm under the LHCP incidence and (f) z = 200 mm under the RHCP incidence, and the insets show the simulated and measured energy distributions in the corresponding *xoy* planes.

shift $\phi^+(x, y)$ or $\phi^-(x, y)$. One should note that the meta-atom would provide a traditional symmetrical phase shifting when $|\phi^+(x, y)| = -|\phi^-(x, y)|$, which may realize the totally antisymmetrical manipulation for orthogonal polarizations. Then, the Jones matrix of the meta-atom at the coordinate (x, y) can be derived as (the detailed derivation process can be found in the Supporting Information)

$$J = \frac{1}{2}\begin{bmatrix} e^{i\cdot\phi^+(x,y)} + e^{i\cdot\phi^-(x,y)} & -i\cdot e^{i\cdot\phi^+(x,y)} + i\cdot e^{i\cdot\phi^-(x,y)} \\ -i\cdot e^{i\cdot\phi^+(x,y)} + i\cdot e^{i\cdot\phi^-(x,y)} & -e^{i\cdot\phi^+(x,y)} - e^{i\cdot\phi^-(x,y)} \end{bmatrix} \quad (1)$$

It can be seen that the Jones matrix is unitary; since J is built based on linear polarization basis, the eigenvalues provide the acquired phase delays δ_x (along x-direction) and δ_y (along y-direction), while the eigenvectors represent the geometric phase (represented by θ) of the meta-atom as follows

$$\delta_x = \frac{1}{2}[e^{i\phi^+(x,y)} + e^{i\phi^-(x,y)}] \quad (2a)$$

$$\delta_y = \frac{1}{2}[e^{i\phi^+(x,y)} + e^{i\phi^-(x,y)}] - \pi \quad (2b)$$

$$\theta = \frac{1}{4}[e^{i\phi^+(x,y)} + e^{i\phi^-(x,y)}] \quad (2c)$$

Phase delays δ_x and δ_y are determined by the physical dimensions of the meta-atom projected in the x- and y-directions, respectively, while the rotation angle θ is defined as the angle between the optical axis and $+x$-axis. Based on eqs 2a−2c, with specific spatial phase distributions $\phi^+(x, y)$ and $\phi^-(x, y)$ for the functionalities of LHCP and RHCP incident waves, respectively, δ_x, δ_y, and θ of a meta-atom located at a specific coordinate can be calculated. Therefore, the second step is to establish a library of meta-atoms to provide the specific phase requirement satisfying eqs 2a−2c for the metasurface design.

Here, the meta-atom utilized is based on the miniaturized element frequency selective surface (MEFSS), which can guarantee a high transmission efficiency within a wide working frequency range.[59] The number of layers and the structure of each metallic layer are initially chosen according to the requirement of the center frequency, fractional bandwidth, and phase coverage, and then optimizations are implemented in full-wave simulations using commercial software CST Microwave Studio to get a high transmission coefficient and specific frequency response. The nonresonant MEFSS meta-atom is composed of five metallic layers to guarantee the phase coverage of 2π, which are separated by four dielectric substrate layers with same thickness; the decomposed topological layouts of the meta-atom structure are illustrated in the inset of Figure 1a. Different from the traditional MEFSS element,[59] three parallel gaps are implemented in each rectangular patch for structure miniaturization, and the circular aperture instead of square grid is adopted in the metallic grid to guarantee polarization insensitivity during the rotation of the meta-atom as required by eq 2c.

Here, for the sake of demonstration, a MEFSS meta-atom (No. 7 in the library as a representative) is picked out to show the EM response, whose construction parameters are given in Table S1 (shown in the Supporting Information). Figure 1b,c depicts the simulated magnitude and phase profile of the transmission spectra under orthogonal linearly polarized incident waves. It can be observed that the amplitudes of both transmission coefficients are higher than 0.9 around the center frequency of 10 GHz, indicating that most of the incident energy is transmitted under the co-polarization mode, while the cross-polarized amplitudes both approach zero, attributed to the symmetrical feature of the proposed meta-atom. The phase difference between two transmitted waves $\Delta\varphi = |\varphi_{xx} - \varphi_{yy}| = \pi$ ($+\pi$ for RHCP, $-\pi$ for LHCP) can be achieved within a wide working frequency band spanning from 8 to 12 GHz, guaranteeing the conversion of the incident CP wave into the cross-polarized state in the transmitted field.

To obtain the full phase range coverage as accurately as possible, a library of 24 meta-atoms is established with

DOI: 10.1021/acsami.9b07102
ACS Appl. Mater. Interfaces 2019, 11, 28423−28430

meticulous optimization, whose simulated phase delays (δ_x and δ_y) and the corresponding phase difference are exhibited in Figure 1d. All 24 meta-atoms endow uniform phase interval of $\pi/12$, and the construction parameters of each meta-atom can be found in Table S1 in the Supporting Information.

Bifunctional Metasurfaces for Independent Manipulation of Orthogonal CP Incidence. Once the two switchable functionalities of the metalens under orthogonal CP incidence are fixed, phase distributions on the metasurface can be calculated based on eqs 2a−2c with ascertained phase profiles $\phi^+(x, y)$ and $\phi^-(x, y)$ (step 1 in the design approach), and meta-atom with suitable phase response can be selected from the library established (step 2 in the design approach) to mimic the spatial phase distributions on the metalens. Through corresponding rotation for each meta-atom as required by eq 2c, bifunctional metalenses can be constructed (step 3 in the design approach). Here, three metalenses are designed to show two independent functions that can be switched by flipping the helicity of the CP incidence.

First, a bifocal converging metalens is proposed, which exhibits switchable focal lengths under orthogonal CP incidence. The proposed metalens can on one hand efficiently focus the RHCP component with a focal length of f_1 = 100 mm under LHCP incidence and, on the other hand, focus the LHCP component with f_2 = 200 mm under the RHCP incidence. The schematic principle for the proposed bifocal converging lens is illustrated in Figure 2a, where the metalens is represented by a metallic patch layer for simplicity. With reference to optical converging lenses, the spatial phase profile is obtained as follows

$$\phi_1^{+}(x, y) = 2\pi(\sqrt{f_1^2 + (x^2 + y^2)} - |f_1|)/\lambda \tag{3a}$$

$$\phi_1^{-}(x, y) = 2\pi(\sqrt{f_2^2 + (x^2 + y^2)} - |f_2|)/\lambda \tag{3b}$$

where λ is the wavelength and f_i (i = 1, 2) is the desired focal length. According to eqs 3a and 3b, different parabolic phase profiles for orthogonal circular polarizations can be calculated as shown in Figure 2b, and the insets express the required phase distributions for different converging performances. By substituting eqs 3a and 3b with different f_i into eqs 2a−2c, the specific phase delays along x- and y-axis and the rotation angle of each meta-atom can be obtained. Then, by utilizing the library of meta-atoms to fit the required phase values, the phase distribution of the metalens for bifocal converging under orthogonal circular polarized incidence can be achieved and demonstrated by the symbols in Figure 2b, which are in good accordance with the theoretical ones.

Simulation and measurement results of the bifocal metalens are displayed in Figure 2c−f. The photography of the prototypes and fabrication process are all detailed in the Supporting Information Text S4, and the near-field mapping measurements are depicted in the Experimental Section. It can be seen from Figure 2c,d that under the LHCP incident wave illumination, the metalens with the total thickness of 4.475 mm ($0.15\lambda_0$ at 10 GHz) can generate a transmitted converged wave with the preset focal length of 100 mm along the propagation direction (+z-axis), and the measured focusing distance agrees well with the theoretical design. To further characterize the performance of convergence, the energy intensity in focal plane at z = 100 mm is provided in Figure 2d. By comparing the cross section and horizontal cuts of the focus spot, the intensity distributions of simulation and measurement are observed to be in good agreement with each other. The full width at half-maxima (FWHMs) of normalized intensity profiles of the focal spot are $0.87\lambda_0$ from simulation and $0.67\lambda_0$ from measurement, indicating that a high-quality focus spot can indeed be produced. Figure 2e,f exhibits the corresponding performances of the metalens under the RHCP incident wave. The measured energy distribution in the xoz and yoz planes clearly show the focal point at z = 200 mm, conforming to the designed focus length f_2 = 200 mm. The FWHMs of the simulated and measured horizontal cuts are $0.87\lambda_0$ and λ_0, respectively, guaranteeing the high-quality focus under RHCP incident wave illumination. This bifocal metalens with switchable focal length under different CP incidence can find potential applications in the microwave near-field imaging for tumor detection and diagnostics.[33]

Second, an OAM generator with a dual-mode functionality is proposed. Two independent OAM modes are generated and switched by flipping the helicity of incident CP wave. A metalens generating vortex beam with OAM modes of l_1 = 3 under the LHCP incidence and l_2 = 1 under the RHCP incidence is illustrated in Figure 3a. To generate a vortex beam

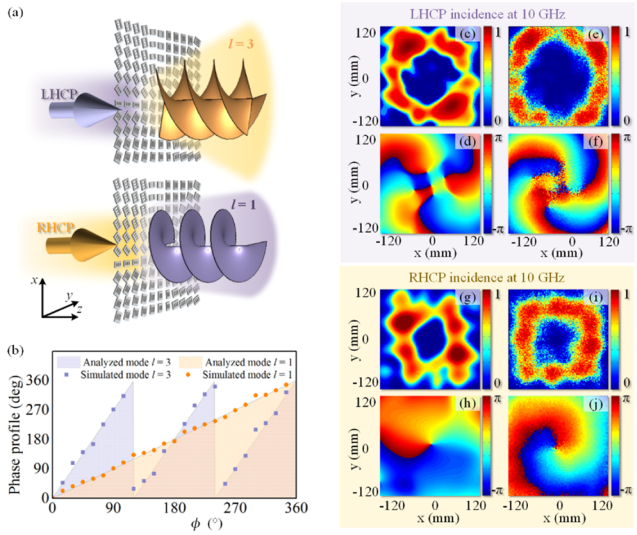

Figure 3. Dual-mode OAM generator based on the metasurface. (a) Schematic principle of the proposed metagenerator, which can produce OAM modes with l = 3 and l = 1 under opposite CP polarizations. (b) Calculated and simulated spatial phase profiles for dual-mode OAM functionality generation. Simulated and measured energy intensity and phase distributions in the xoy plane at z = 150 mm under (c−f) the LHCP incidence and (g−j) the RHCP incidence.

carrying the OAM mode, it is obvious that the phase factor should be introduced in the azimuthal direction

$$\phi_2^{+}(x, y) = l_1 \cdot \arctan(y/x) \tag{4a}$$

$$\phi_2^{-}(x, y) = l_2 \cdot \arctan(y/x) \tag{4b}$$

where l_i (i = 1, 2) expresses the topological charge of OAM mode. To distinguish the OAM modes with orthogonal CP, the spatial phase profiles of the OAM modes with l_1 = 3 and l_2 = 1 can be deduced, as depicted in Figure 3b. By calculating the required phase delays for orthogonal linear polarizations and rotation angles, the phase distribution can be fitted with 24

DOI: 10.1021/acsami.9b07102
ACS Appl. Mater. Interfaces 2019, 11, 28423−28430

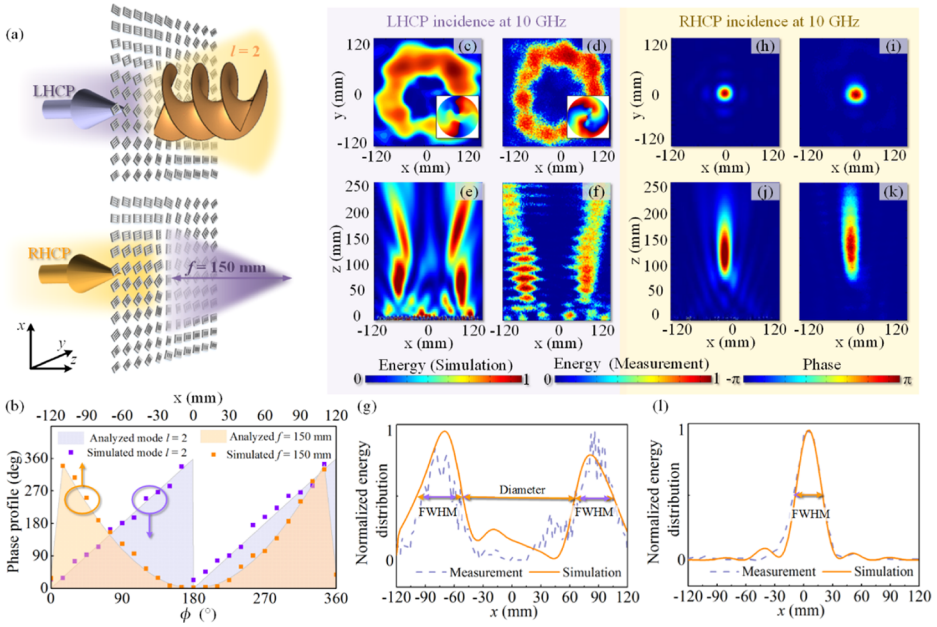

Figure 4. Switchable beam between vortex beam and converging beam based on metasurface. (a) Schematic principle of metalens for generating different functions depending on polarization state. (b) Calculated and simulated spatial phase profiles for a vortex beam with the OAM mode of l = 2 and a converging beam with a focal length of f = 150 mm. Under the LHCP incidence, (c, d) show simulated and measured energy distributions at z = 150 mm in the *xoy* plane, respectively, where the insets illustrate the corresponding phase distributions and (e, f) show the simulated and measured energy distributions in the *xoz* plane. Under RHCP incidence, (h, i) depict the simulated and measured energy distributions in the *xoy* plane at z = 150 mm. (j, k) Simulated and measured energy distributions in the *xoz* plane. Simulated and measured normalized energy intensity of the horizontal cuts in the *xoy* plane at z = 150 mm for (g) LHCP and (l) RHCP illuminations, respectively.

meta-atoms, as shown by symbols in Figure 3b, and the dual-mode functionality of the OAM generator can be constructed.

Figure 3c–f shows the simulation and measurement results of the OAM generator upon LHCP incidence illumination. The legible doughnut-shape energy distribution is presented in both simulated (z = 150 mm; Figure 3c) and measured *xoy* planes (z = 150 mm; Figure 3e), while the simulated (Figure 3d) and measured phase distributions (Figure 3f) both exhibit three helical twists patterns corresponding to the theoretical phase change of l*2π. It is revealed that the proposed metalens can convert the LHCP incidence into vortex beam with the OAM mode l_1 = 3 as desired. Upon RHCP illumination, Figure 3g,h depicts the simulated response profiles at z = 150 mm in the *xoy* plane, where the doughnut-shape energy distribution and one helical twist phase pattern verify the generation of the OAM mode l_2 = 1. Apart from a slight difference in intensity and inhomogeneity, the measured energy and phase distributions presented in Figure 3i,j qualitatively agree with simulation results, indicating that the vortex beam with the OAM mode l_2 = 1 can be indeed generated under the RHCP incidence. This metalens with the function of switchable dual-mode OAM generation can be potentially applied to build reconfigurable antennas for OAM multiplexing in the microwave region.

The observed nonuniform energy distributions in the *xoy* plane are attributed to the nonconstant transmission amplitudes of all 24 meta-atoms used to construct the metalens, as specifically explained in the Supporting Information Text S5. Additionally, the step size of the field mapping measurement is ten times the mesh used in the FDTD simulation, so the number of pixels in the measured intensity and phase maps are only 1% of that in the simulated maps (the measurement process is illustrated in the Experimental Section). This makes the measurement results seem a little bit rough compared with the simulation results. Furthermore, noises observed in the measured data are due to low reflections from the metallic translation stages supporting the field-sensing probe.

Finally, beam switching between different functionalities depending on the polarization state of the incident wave is demonstrated by the proposed scheme. Figure 4a illustrates a bifunctional metalens as a proof-of-concept generating a vortex beam/converging beam under the LHCP/RHCP incidence, respectively. The phase profile for the LHCP incidence is calculated by a spiral phase plate, while that for the RHCP incidence is analyzed by a converging lens, which can be described as

$$\phi_3^{+}(x, y) = l\cdot\arctan(y/x) \tag{5a}$$

$$\phi_3^{-}(x, y) = 2\pi(\sqrt{f^2 + (x^2 + y^2)} - |f|)/\lambda \tag{5b}$$

The required phase profiles for totally independent functions, shown in Figure 4b, can be integrated into our proposed metalens. Figure 4c–g presents the vortex beam carrying the OAM mode l = 2 generated by the proposed metalens under the LHCP incidence, while the results of the converging beam with the focal length f = 150 mm produced under the RHCP incidence are exhibited in Figure 4h–l. Figure 4c depicts the simulated energy intensity in the *xoy* plane at z = 150 mm, where a clear doughnut-shape energy ring representing the generation of vortex beam and the helical phase pattern distribution in the inset can be observed. Corresponding measurement results of the intensity and helical phase distributions are illustrated in Figure 4d, showing good agreement with the numerical simulations. Figure 4e,f presents the simulated and measured energy intensities at a cross

DOI: 10.1021/acsami.9b07102
ACS Appl. Mater. Interfaces 2019, 11, 28423–28430

section along the propagation direction (*xoz* plane with $y = 0$). The hollow and divergent characteristics further verify the generation of vortex beam under the LHCP incidence. Figure 4g presents the simulated and measured horizontal cuts of normalized energy intensity at $z = 150$ mm in the *xoy* plane, and two peaks in the profile represent the energy annulus, where the average FWHMs are about $1.27\lambda_0$ (simulation) and $1.2\lambda_0$ (measurement) and the simulated and measured diameters of the annuluses are $4.07\lambda_0$ and $4.2\lambda_0$. For comparison, with the RHCP incidence, the simulated and measured intensities in the focal plane at $z = 150$ mm (*xoy* plane) are shown in Figure 4h,i, while that at the cross section along the *z*-axis are presented in Figure 4j,k, inferring that the cross-polarized transmitted wave is properly converted into a converging beam. The focus quality can be evaluated by its horizontal cut of normalized energy intensity in the focal plane at $z = 150$ mm, as depicted in Figure 4l. The simulated and measured FWHMs are $0.93\lambda_0$ and $0.9\lambda_0$, respectively, indicating the high quality of the converging beam generated by the proposed metalens.

The above simulated and measured performances validate the bifunctional characteristics of the designed metalenses. Furthermore, the working bandwidth is another evaluation criterion of the proposed metalenses. Here, the bandwidth is acquired by both the transmission performance and the phase coverage of the meta-atom, which can be considered as an equivalent filter[59] and thus the bandwidth is related to the order of the filter. Herein, all the proposed three metalenses can exhibit excellent performances within the 9−11 GHz frequency band, and the corresponding simulated and measured results are given in the Supporting Information Text S3. The bandwidth could be further enhanced by the multilayered structure of the meta-atom, but at the cost of higher thickness.

Transmission Efficiency. As a key factor for transmission-type metalenses, the transmission efficiency is evaluated and defined as the ratio between the energy carried by cross-polarized transmitted wave and that carried by incident wave, which can be described as

$$\eta = \frac{P_{\text{cross-pol}}}{P_{\text{incidence}}} = \frac{\int |\vec{E}_{\text{cross-pol}}|^2 \mathrm{d}s}{\int |\vec{E}_{\text{incidence}}|^2 \mathrm{d}s} \tag{6}$$

where s is the area of the measured plane, $P_{\text{cross-pol}}$ is the cross-polarized energy in the transmission field, and $P_{\text{incidence}}$ is the incident energy. The measured transmission efficiencies of three proposed metalenses are illustrated in Figure 5, and the specific calculation method can be found in the Supporting Information Text S5. It can be found that the incident CP can be transmitted into its reverse handedness with a high efficiency of around 80% in the bandwidth of 9.5−10.5 GHz (relative bandwidth is 10%), indicating that most incident energy can be utilized to achieve the required performance in the transmission mode. Furthermore, it can be observed that the measured peak value of the efficiencies of the proposed MEFSS metadevices are about 81, 85, and 93% at around 10 GHz, which guarantee high performances of the required functionalities. However, there are inevitable losses caused by reflections from the measurement setup and by nonuniform transmission amplitudes of all the 24 meta-atoms, which are discussed in detail in the Supporting Information Text S5. Nevertheless, compared to previous results on transmission-type metasurfaces,[46,47,52,57] a good trade-off is obtained to achieve an efficiency of over 80% by utilizing ultrathin metalens with a fabricated thickness of only $0.15\lambda_0$.

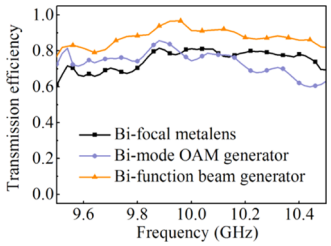

Figure 5. Measured transmission efficiency of the three proposed metalenses. Peak efficiency higher than 80% can be observed near 10 GHz for the different proposed designs.

Conclusions. A general paradigm to design high-efficiency transmission-type metasurface with switchable functionalities is proposed in this paper. Three metalenses are presented to demonstrate that two independent functions can be switched by flipping the helicity of the incident CP waves, which overcome antisymmetrical characteristics limits between orthogonal CP incidences achieved by metalenses based on solely geometric phase. Both full-wave simulations and measurements show that the proposed metalenses have successfully realized the predicted functionalities, including switchable focal-length, dual-mode OAM and switchable beam between converging beam and vortex beam. Furthermore, all ultrathin metadevices show high transmission efficiency within a broad frequency range. The proposed metadevices in this paper can find potential applications in reconfigurable lenses and antennas for microwave communication systems.

METHODS

Experimental Section. The schematic of the near-field measurement system is exhibited in Figure S4a, which is mainly composed of a feeding source antenna, field probe, vector network analyzer and motion controller. The measurements are conducted by a setup surrounded by absorbers to minimize parasitic reflections. The feeding source is a dual-polarized wideband horn antenna, launching the quasi-plane wave within the frequency band from 2 to 18 GHz (left-handed circular polarization (LHCP) and right-handed circular polarization (RHCP) as required). Here, to keep the incident wave to be a quasi-plane wave as used in the full wave simulation, the distance between the horn antenna and the metalens is set to be over $20\lambda_0$. A fiber optic active antenna, which is purely a dielectric probe connected to an optical fiber cable, is used as a field probe to measure the electric field at each pixel. Compared to a metallic probe, the probe we used eliminates the possibility of having scattered field on metallic elements and coaxial cables and thus gives relatively accurate measurement results. The dielectric probe and the source horn antenna are both connected to an Agilent 8722ES vector network analyzer, which can measure and record both amplitude and phase of the complex S_{21} and S_{11} parameters. Here, the transmission coefficient and reflection coefficient of the system under test are expressed by S_{21} and S_{11} parameters, respectively. The dielectric probe is oriented in two orthogonal directions, and then the two components (horizontal and vertical) of the electric field can be measured and recorded at one fixed pixel, which will be further used to calculate the CP field, including both amplitude and phase. The position of this probe is fixed on two translation stages controlled by a motion controller and is incremented by a step of 2 mm to totally cover the *xoy* and *xoz* planes to be measured.

DOI: 10.1021/acsami.9b07102
ACS Appl. Mater. Interfaces 2019, 11, 28423−28430

■ ASSOCIATED CONTENT

Supporting Information

The Supporting Information is available free of charge on the ACS Publications website at DOI: 10.1021/acsami.9b07102.

Derivation of Jones matrix; construction parameters of meta-atoms; broadband performance of the proposed metalenses; fabrication; and evaluation of transmission efficiency (PDF)

■ AUTHOR INFORMATION

Corresponding Authors

*E-mail: zhangkuang@hit.edu.cn (K.Z.).
*E-mail: xuminding@hit.edu.cn (X.D.).
*Email: sburokur@parisnanterre.fr (S.N.B.).

ORCID

Kuang Zhang: 0000-0002-5642-967X
Xumin Ding: 0000-0002-7725-790X
Shah Nawaz Burokur: 0000-0002-1848-4862

Funding

This work is supported by National Natural Science Foundation of China (Nos. 61771172 and 61401122).

Notes

The authors declare no competing financial interest.

■ REFERENCES

(1) Pfeiffer, C.; Grbic, A. Cascaded Metasurfaces for Complete Phase and Polarization Control. *Appl. Phys. Lett.* **2013**, *102*, No. 231116.

(2) Jiang, S.-C.; Xiong, X.; Sarriugarte, P.; Jiang, S.-W.; Yin, X.-B.; Wang, Y.; Peng, R.-W.; Wu, D.; Hillenbrand, R.; Zhang, X.; Wang, M. Tuning the Polarization State of Light via Time Retardation with a Microstructured Surface. *Phys. Rev. B* **2013**, *88*, No. 239903.

(3) Lei, Z.; Yang, T. Converting State of Polarization with a Miniaturized Metasurface device. *IEEE Photonics Technol. Lett.* **2017**, *29*, 615−618.

(4) Yurduseven, O.; Marks, D. L.; Fromenteze, T.; Smith, D. R. Dynamically Reconfigurable Holographic Metasurface Aperture for a Mills-Cross Monochromatic Microwave Camera. *Opt. Express* **2018**, *26*, 5281−5291.

(5) Jiang, Q.; Bao, Y.; Lin, F.; Zhu, X.; Zhang, S.; Fang, Z. Spin-Controlled Integrated Near-and Far-Field Optical Launcher. *Adv. Funct. Mater.* **2018**, *28*, No. 1705503.

(6) Xiao, S.; Mühlenbernd, H.; Li, G.; Kenney, M.; Liu, F.; Zentgraf, T.; Zhang, S.; Li, J. Helicity-Preserving Omnidirectional Plasmonic Mirror. *Adv. Opt. Mater.* **2016**, *4*, 654−658.

(7) Zhang, L.; Mei, S.; Huang, K.; Qiu, C. W. Advances in Full Control of Electromagnetic Waves with Metasurfaces. *Adv. Opt. Mater.* **2016**, *4*, 818−833.

(8) Qin, F.; Ding, L.; Zhang, L.; Monticone, F.; Chum, C. C.; Deng, J.; Mei, S.; Li, Y.; Teng, J.; Hong, M.; Zhang, S.; Alu, A.; Qiu, C. W. Hybrid Bilayer Plasmonic Metasurface Efficiently Manipulates Visible Light. *Sci. Adv.* **2016**, *2*, No. e1501168.

(9) Chen, X.; Zhang, Y.; Huang, L.; Zhang, S. Ultrathin Metasurface Laser Beam Shaper. *Adv. Opt. Mater.* **2014**, *2*, 978−982.

(10) Zhu, A. Y.; Chen, W.-T.; Khorasaninejad, M.; Oh, J.; Zaidi, A.; Mishra, I.; Devlin, R. C.; Capasso, F. Ultra-Compact Visible Chiral Spectrometer with Meta-lenses. *APL Photonics* **2017**, *2*, No. 036103.

(11) Cong, L.; Xu, N.; Zhang, W.; Singh, R. Polarization Control in Terahertz Metasurfaces with the Lowest Order Rotational Symmetry. *Adv. Opt. Mater.* **2015**, *3*, 1176−1183.

(12) Zeng, J.; Li, L.; Yang, X.; Gao, J. Generating and Separating Twisted Light by Gradient-Rotation Split-Ring Antenna Metasurfaces. *Nano Lett.* **2016**, *16*, 3101−3108.

(13) Karimi, E.; Schulz, S. A.; De Leon, I.; Qassim, H.; Upham, J.; Boyd, R. W. Generating Optical Orbital Angular Momentum at Visible Wavelengths Using a Plasmonic Metasurface. *Light: Sci. Appl.* **2014**, *3*, No. e167.

(14) Li, G.; Wu, L.; Li, K. F.; Chen, S.; Schlickriede, C.; Xu, Z.; Huang, S.; Li, W.; Liu, Y.; Pun, E. Y.; et al. Nonlinear Metasurface for Simultaneous Control of Spin and Orbital Angular Momentum in Second Harmonic Generation. *Nano Lett.* **2017**, *17*, 7974−7979.

(15) Mehmood, M.; Mei, S.; Hussain, S.; Huang, K.; Siew, S.; Zhang, L.; Zhang, T.; Ling, X.; Liu, H.; Teng, J.; Danner, A.; Zhang, S.; Qiu, C. W. Visible-Frequency Metasurface for Structuring and Spatially Multiplexing Optical Vortices. *Adv. Mater.* **2016**, *28*, 2533−2539.

(16) Arbabi, A.; Horie, Y.; Bagheri, M.; Faraon, A. Dielectric Metasurfaces for Complete Control of Phase and Polarization with Subwavelength Spatial Resolution and High Transmission. *Nat. Nanotechnol.* **2015**, *10*, 937.

(17) Wang, L.; Kruk, S.; Tang, H.; Li, T.; Kravchenko, I.; Neshev, D. N.; Kivshar, Y. S. Grayscale Transparent Metasurface Holograms. *Optica* **2016**, *3*, 1504−1505.

(18) Wen, D.; Yue, F.; Li, G.; Zheng, G.; Chan, K.; Chen, S.; Chen, M.; Li, K. F.; Wong, P. W. H.; Cheah, K. W.; et al. Helicity Multiplexed Broadband Metasurface Hograms. *Nat. Commun.* **2015**, *6*, No. 8241.

(19) Yifat, Y.; Eitan, M.; Iluz, Z.; Hanein, Y.; Boag, A.; Scheuer, J. Highly Efficient and Broadband Wide-angle Holography Using Patch-Dipole Nanoantenna Reflectarrays. *Nano Lett.* **2014**, *14*, 2485−2490.

(20) Li, X.; Chen, L.; Li, Y.; Zhang, X.; Pu, M.; Zhao, Z.; Ma, X.; Wang, Y.; Hong, M.; Luo, X. Multicolor 3D Meta-Holography by Broadband Plasmonic Modulation. *Sci. Adv.* **2016**, *2*, No. e1601102.

(21) Qing, Y. M.; Ma, H. F.; Cui, T. J. Investigation of Strong Multimode Interaction in a Graphene-Based Hybrid Coupled Plasmonic System. *Carbon* **2019**, *145*, 596−602.

(22) Yu, P.; Li, J.; Zhang, S.; Jin, Z.; Schütz, G.; Qiu, C.; Hirscher, M.; Liu, N. Dynamic Janus Metasurfaces in the Visible Spectral Region. *Nano Lett.* **2018**, *18*, 4584−4589.

(23) Cong, L.; Xu, N.; Han, J.; Zhang, W.; Singh, R. A Tunable Dispersion-Free Terahertz Metadevice with Pancharatnam-Berry-Phase-Enabled Modulation and Polarization Control. *Adv. Mater.* **2015**, *27*, 6630−6636.

(24) Cong, L.; Pitchappa, P.; Wu, Y.; Ke, L.; Lee, C.; Singh, N.; Yang, H.; Singh, R. Active Multifunctional Microelectromechanical System Metadevices: Applications in Polarization Control, Wavefront Deflection, and Holograms. *Adv. Opt. Mater.* **2017**, *5*, No. 1600716.

(25) Cong, L.; Pitchappa, P.; Lee, C.; Singh, R. Active Phase Transition via Loss Engineering in a Terahertz MEMS Metamaterial. *Adv. Mater.* **2017**, *29*, No. 1700733.

(26) Cong, L.; Srivastava, Y. K.; Zhang, H.; Zhang, X.; Han, J.; Singh, R. All-Optical Active THz Metasurfaces for Ultrafast Polarization Switching and Dynamic Beam Splitting. *Light: Sci. Appl.* **2018**, *7*, 28.

(27) Cong, L.; Pitchappa, P.; Wang, N.; Singh, R. Electrically Programmable Terahertz Diatomic Metamolecules for Chiral Optical Control. *Research* **2019**, *2019*, No. 7084251.

(28) Li, Y.; Zhang, J.; Qu, S.; Wang, J.; Chen, H.; Xu, Z.; Zhang, A. Wideband Radar Cross Section Reduction Using Two-Dimensional Phase Gradient Metasurfaces. *Appl. Phys. Lett.* **2014**, *104*, No. 221110.

(29) Huang, C.; Pan, W.; Ma, X.; Luo, X. Wideband Radar Cross-Section Reduction of a Stacked Patch Array Antenna Using Metasurface. *IEEE Antennas Wirel. Propag. Lett.* **2015**, *14*, 1369−1372.

(30) Ma, H. F.; Shen, X.; Cheng, Q.; Jiang, W. X.; Cui, T. J. Broadband and High-Efficiency Conversion from Guided Waves to Spoof Surface Plasmon Polaritons. *Laser Photonics Rev.* **2014**, *8*, 146−151.

(31) Yan, L.; Zhu, W.; Karim, M. F.; Cai, H.; Gu, A. Y.; Shen, Z.; Chong, P. H. J.; Kwong, D. L.; Qiu, C. W.; Liu, A. Q. 0.2 λ_0 Thick Adaptive Retroreflector Made of Spin-Locked Metasurface. *Adv. Mater.* **2018**, *30*, No. 1802721.

(32) Sleasman, T.; Boyarsky, M.; Imani, M. F.; Fromenteze, T.; Gollub, J. N.; Smith, D. R. Single-Frequency Microwave Imaging with

DOI: 10.1021/acsami.9b07102
ACS Appl. Mater. Interfaces 2019, 11, 28423−28430

Dynamic Metasurface Apertures. *J. Opt. Soc. Am. B* **2017**, *34*, 1713−1726.
(33) Bond, E. J.; Li, X.; Hagness, S. C.; Van Veen, B. D. Microwave Imaging via Space-Time Beamforming for Early Detection of Breast Cancer. *IEEE Trans. Antennas Propag.* **2003**, *51*, 1690−1705.
(34) Wang, G.; Gong, Y. Metamaterial Lens Applicator for Microwave Hyperthermia of Breast Cancer. *Int. J. Hyperthermia* **2009**, *25*, 434−445.
(35) Gong, Y.; Wang, G. Superficial Tumor Hyperthermia with Flat Left-Handed Metamaterial Lens. *Prog. Electromagn. Res.* **2009**, *98*, 389−405.
(36) Orazbayev, B.; Mohammadi Estakhri, N.; Alù, A.; Beruete, M. Experimental Demonstration of Metasurface-Based Ultrathin Carpet Cloaks for Millimeter Waves. *Adv. Opt. Mater.* **2017**, *5*, No. 1600606.
(37) Yang, Y.; Jing, L.; Zheng, B.; Hao, R.; Yin, W.; Li, E.; Soukoulis, C. M.; Chen, H. Full-Polarization 3D Metasurface Cloak with Preserved Amplitude and Phase. *Adv. Mater.* **2016**, *28*, 6866−6871.
(38) Aghanejad, I.; Abiri, H.; Yahaghi, A. Design of High-Gain Lens Antenna by Gradient-Index Metamaterials Using Transformation Optics. *IEEE Trans. Antennas Propag.* **2012**, *60*, 4074−4081.
(39) Abbaspour-Tamijani, A.; Zhang, L.; Pan, G.; Pan, H. K.; Alavi, H. In *Lens-Enhanced Phased Array Antenna System for High Directivity Beam-Steering*, 2011 IEEE International Symposium on Antennas and Propagation (APSURSI), Spokane, WA, 2011; pp 3275−3278.
(40) Tamburini, F.; Mari, E.; Sponselli, A.; Thidé, B.; Bianchini, A.; Romanato, F. Encoding Many Channels on the Same Frequency Through Radio Vorticity: First Experimental Test. *New J. Phys.* **2012**, *14*, No. 033001.
(41) Mohammadi, S. M.; Daldorff, L. K.; Bergman, J. E.; Karlsson, R. L.; Thidé, B.; Forozesh, K.; Carozzi, T. D.; Isham, B. Orbital Angular Momentum in Radio — A System Study. *IEEE Trans. Antennas Propag.* **2010**, *58*, 565−572.
(42) Zhang, K.; Yuan, Y.; Zhang, D.; Ding, X.; Ratni, B.; Burokur, S. N.; Lu, M.; Tang, K.; Wu, Q. Phase-Engineered Metalenses to Generate Converging and Non-Diffractive Vortex Beam Carrying Orbital Angular Momentum in Microwave Region. *Opt. Express* **2018**, *26*, 1351−1360.
(43) Monticone, F.; Estakhri, N. M.; Alù, A. Full Control of Nanoscale Optical Transmission with a Composite Metascreen. *Phys. Rev. Lett.* **2013**, *110*, No. 203903.
(44) Asadchy, V. S.; Ra'Di, Y.; Vehmas, J.; Tretyakov, S. Functional Metamirrors Using Bianisotropic Elements. *Phys. Rev. Lett.* **2015**, *114*, No. 095503.
(45) Yu, S.; Li, L.; Shi, G.; Zhu, C.; Shi, Y. Generating Multiple Orbital Angular Momentum Vortex Beams Using a Metasurface in Radio Frequency Domain. *Appl. Phys. Lett.* **2016**, *108*, No. 241901.
(46) Zhang, H.; Zhang, X.; Xu, Q.; Tian, C.; Wang, Q.; Xu, Y.; Li, Y.; Gu, J.; Tian, Z.; Ouyang, C.; et al. High-Efficiency Dielectric Metasurfaces for Polarization-Dependent Terahertz Wavefront Manipulation. *Adv. Opt. Mater.* **2018**, *6*, No. 1700773.
(47) Cai, T.; Tang, S.; Wang, G.; Xu, H.; Sun, S.; He, Q.; Zhou, L. High-Performance Bifunctional Metasurfaces in Transmission and Reflection Geometries. *Adv. Opt. Mater.* **2017**, *5*, No. 1600506.
(48) Ma, Z.; Li, Y.; Li, Y.; Gong, Y.; Maier, S. A.; Hong, M. All-Dielectric Planar Chiral Metasurface with Gradient Geometric Phase. *Opt. Express* **2018**, *26*, 6067−6078.
(49) Xu, H.-X.; Liu, H.; Ling, X.; Sun, Y.; Yuan, F. Broadband Vortex Beam Generation Using Multimode Pancharatnam−Berry Metasurface. *IEEE Trans. Antennas Propag.* **2017**, *65*, 7378−7382.
(50) Maguid, E.; Yulevich, I.; Yannai, M.; Kleiner, V.; Brongersma, M. L.; Hasman, E. Multifunctional Interleaved Geometric-Phase Dielectric Metasurfaces. *Light: Sci. Appl.* **2017**, *6*, No. e17027.
(51) Zhang, L.; Liu, S.; Li, L.; Cui, T. J. Spin-Controlled Multiple Pencil Beams and Vortex Beams with Different Polarizations Generated by Pancharatnam-Berry Coding Metasurfaces. *ACS Appl. Mater. Interfaces* **2017**, *9*, 36447−36455.
(52) Ding, X.; Monticone, F.; Zhang, K.; Zhang, L.; Gao, D.; Burokur, S. N.; de Lustrac, A.; Wu, Q.; Qiu, C. W.; Alù, A. Ultrathin Pancharatnam−Berry Metasurface with Maximal Cross-Polarization Efficiency. *Adv. Mater.* **2015**, *27*, 1195−1200.
(53) Lin, D.; Holsteen, A. L.; Maguid, E.; Wetzstein, G.; Kik, P. G.; Hasman, E.; Brongersma, M. L. Photonic Multitasking Interleaved Si Manoantenna Phased Array. *Nano Lett.* **2016**, *16*, 7671−7676.
(54) Khorasaninejad, M.; Chen, W.-T.; Zhu, A. Y.; Oh, J.; Devlin, R.; Rousso, D.; Capasso, F. Multispectral Chiral Imaging with a Metalens. *Nano Lett.* **2016**, *16*, 4595−4600.
(55) Mueller, J. B.; Rubin, N. A.; Devlin, R. C.; Groever, B.; Capasso, F. Metasurface Polarization Optics: Independent Phase Control of Arbitrary Orthogonal States of Polarization. *Phys. Rev. Lett.* **2017**, *118*, No. 113901.
(56) Devlin, R. C.; Ambrosio, A.; Rubin, N. A.; Mueller, J. B.; Capasso, F. Arbitrary Spin-to−Orbital Angular Momentum Conversion of Light. *Science* **2017**, *358*, 896−901.
(57) Wang, B.; Dong, F.; Feng, H.; Yang, D.; Song, Z.; Xu, L.; Chu, W.; Gong, Q.; Li, Y. Rochon-Prism-Like Planar Circularly Polarized Beam Splitters Based on Dielectric Metasurfaces. *ACS Photonics* **2018**, *5*, 1660−1664.
(58) Groever, B.; Rubin, N. A.; Mueller, J. B.; Devlin, R. C.; Capasso, F. High-Efficiency Chiral Meta-Lens. *Sci. Rep.* **2018**, *8*, No. 7240.
(59) Al-Joumayly, M. A.; Behdad, N. A Generalized Method for Synthesizing Low-Profile, Band-Pass Frequency Selective Surfaces with Non-Resonant Constituting Elements. *IEEE Trans. Antennas Propag.* **2010**, *58*, 4033−4041.

DOI: 10.1021/acsami.9b07102
ACS Appl. Mater. Interfaces 2019, 11, 28423−28430